Research Square

Preprints are preliminary reports that have not undergone peer review.
They should not be considered conclusive, used to inform clinical practice,
or referenced by the media as validated information.

In situ acoustic manufacturing of conformal brain–computer interfaces

Shuangquan Gou
The Chinese University of Hong Kong (Shenzhen)
Peikun Mo
Shenzhen Univerisy
Wenliang Liu
Shenzhen Institute for Drug Control
Rao Liu
Shenzhen Institute for Drug Control
Yifang Wang
The Chinese University of Hong Kong (Shenzhen)
Rui Yang
The Chinese University of Hong Kong (Shenzhen)
Caihong Liu
The Chinese University of Hong Kong (Shenzhen)
Chang He
The Chinese University of Hong Kong (Shenzhen)
Anyu Wang
The Chinese University of Hong Kong (Shenzhen)
Lingfei Ma
The Chinese University of Hong Kong (Shenzhen)
Jinde Zhang
The Chinese University of Hong Kong (Shenzhen)
Wenbu Lu
Shanxi Normal University
Jiahao Li
The Chinese University of Hong Kong (Shenzhen)
Hao Li
The Chinese University of Hong Kong (Shenzhen)
Xing HAN
Sun Yat-sen Univeristy https://orcid.org/0000-0001-9052-880X
Shan Liu
Sichuan Academy of Medical Sciences & Sichuan Provincial People's Hospital, University of Electronic Science and Technology of China

Cheng Jiang
The Chinese University of Hong Kong, Shenzhen
Chenzhong Li
chenzhongbiosensor@gmail.com

The Chinese University of Hong Kong (Shenzhen)

Article

Keywords:

Posted Date: November 3rd, 2026

DOI: https://doi.org/10.21203/rs.3.rs-11190892/v1

License: This work is licensed under a Creative Commons Attribution 4.0 International License.
Read Full License

Additional Declarations:
There is **NO** Competing Interest.

Ethical Statement All animal procedures were reviewed and approved by the Animal Management Committee of The Chinese University of Hong Kong, Shenzhen (Approval No. CUHKSZ-D-20250007). All experiments were performed in accordance with institutional guidelines and the National Research Council's Guide for the Care and Use of Laboratory Animals. Animals were housed under standard laboratory conditions with controlled temperature, humidity, and light/dark cycles, and all efforts were made to minimize animal discomfort and the number of animals used.

In situ acoustic manufacturing of conformal brain–computer interfaces

Shuangquan Gou[1], Peikun Mo[2], Wenliang Liu[3], Rao Liu[3], Yifan Wang[1], Rui Yang[1], Caihong Liu[1], Chang He[1], Anyu Wang[1], Lingfei Ma[1], Jinde Zhang[1], Wenbu Lu[4], Jiahao Li[1], Hao Li[1], Xing Han[5]*, Shan Liu[6]*, Cheng Jiang[1]*, Chen-zhong Li[1]*

Affiliations:

[1] Department of Biomedical Engineering, School of Medicine, The Chinese University of Hong Kong (Shenzhen); Shenzhen 518172, China.

[2] Department of Biomedical Engineering, Shenzhen University; Shenzhen 518172, China.

[3] Shenzhen Institute for Drug Control; Shenzhen 518172, China.

[4] Key Laboratory of Magnetic Molecules and Magnetic Information Materials (Ministry of Education), School of Chemistry and Chemical Engineering, Shanxi Normal University; Taiyuan 030031, China.

[5] School of Biomedical Engineering, Shenzhen Campus of Sun Yat-sen University, Sun Yat-sen University, No.66, Gongchang Road, Guangming District, Shenzhen, Guangdong 518107, P. R. China

[6] Sichuan Provincial Key Laboratory for Human Disease Gene Study, Department of Medical Genetics, Sichuan Academy of Medical Sciences & Sichuan Provincial People's Hospital, University of Electronic Science and Technology of China, Chengdu, 610072, China.

*Corresponding author. hanx83@mail.sysu.edu.cn; shanliusyy@uestc.edu.cn; jiangcheng@cuhk.edu.cn; lichenzhong@cuhk.edu.cn

Abstract: Brain–computer interfaces are usually prefabricated and surgically implanted, creating mechanical mismatch, tissue manipulation, inflammation, and signal instability. We report AI-guided in situ ultrasound printing (AiUP), a closed-loop acoustic manufacturing strategy that prints conformal cortical electrodes directly on the dura or brain surface. AiUP integrates pressure-programmable fluorinated silk fibroin nanocages, modular conductive ultrasound-printable inks, ultrasound imaging–guided focused-ultrasound hardware, and an AI controller, EchoAgent. Nanocages collapsed at defined acoustic pressures to release crosslinkers and trigger localized, nonthermal hydrogel formation, whereas EchoAgent planned trajectories, compensated acoustic distortion, and corrected path drift. AiUP produced conductive hydrogel electrodes with ~200 μm resolution, 30 s gelation, ~20 kΩ impedance, 3-month recording stability, and enabled rodent seizure warning and pig neural decoding.

Main Text:

Brain–computer interfaces have transformed neuroscience, neuroprosthetics, epilepsy monitoring, cortical mapping, and closed-loop neuromodulation[1-4]. Yet most implantable neural interfaces still rely on a conventional workflow: electrodes are manufactured outside the body and subsequently implanted onto or into neural tissue[5-7]. This prefabrication–implantation paradigm creates an intrinsic mismatch between a fixed device and a living brain[8, 9]. The cortical surface is curved, hydrated, soft, pulsatile, and individually variable, whereas prefabricated electrode arrays possess predetermined geometries and must be mechanically positioned during surgery[10-12]. As a result, even flexible electrodes may suffer from imperfect conformity, interfacial sliding, micromotion-induced injury, inflammatory encapsulation, impedance drift, and progressive loss of recording fidelity.

An alternative strategy is to fabricate the neural interface directly at the target site. In situ manufacturing could allow electrodes to form according to local anatomy, match tissue mechanics from the moment of formation, and reduce forceful manipulation of fragile neural surfaces[13-15]. However, the brain imposes stringent constraints on such a strategy. Optical curing is limited by scattering and shallow penetration[16-18]. Thermal curing is undesirable because neural tissue is highly sensitive to temperature elevation[16, 19]. Extrusion or direct-write printing requires mechanical access and may perturb delicate tissue[20, 21]. Moreover, skull, dura, cerebrospinal fluid, tissue heterogeneity, and physiological motion distort acoustic fields, making open-loop fabrication unreliable[16, 22]. Thus, a central bottleneck in brain–computer interface engineering is not simply how to make softer electrodes, but how to manufacture patient-specific, mechanically matched neural interfaces directly on neural tissue with remote actuation, real-time imaging, and adaptive control.

Ultrasound offers a potential route to this goal because it penetrates biological tissues more deeply than light, can be focused on space, and is already used for clinical imaging and therapy[23, 24]. However, the unresolved scientific problem is how to couple deep-tissue acoustic energy, pressure-programmable material transformation, real-time image feedback, and adaptive control into a single manufacturing process that can form a functional neural interface in vivo[16, 24]. To transform ultrasound into a manufacturing tool for neural interfaces, several scientific and engineering questions must be solved[25, 26]. First, can acoustic pressure be converted into a programmable mechanochemical signal that initiates localized, nonthermal crosslinking? Second, can the printing process be visualized and actuated within a single ultrasound platform so that ink location, tissue anatomy, focal position, and structure formation are registered in real time? Third, can an intelligent controller compensate for tissue-induced acoustic distortion, physiological motion, and path drift during fabrication? Fourth, can such a system fabricate functional cortical electrodes in vivo and support stable neural recording and decoding in both small and large animals?

We developed AI-guided in situ ultrasound printing, termed AiUP, to address these questions. AiUP integrates pressure-programmable ultrasound-responsive elements[27, 28], modular conductive ultrasound-printable inks, ultrasound imaging–guided focused-ultrasound hardware, and a closed-loop AI controller named EchoAgent [29]. Fluorinated silk fibroin hollow nanocages collapsed at defined acoustic-pressure thresholds of approximately 0.4, 1.3, and 2.8 MPa, enabling selective crosslinker release and localized nonthermal hydrogel formation. Thus, acoustic pressure was converted from a nonspecific energy input into a programmable mechanochemical trigger. The resulting US-Ink was injectable before activation and formed conductive hydrogel electrodes after focused-ultrasound printing. Under optimized conditions,

AiUP achieved approximately 200 μm lateral resolution, gelation within 30 s, electrode impedance of approximately 20 kΩ at 1 kHz, and stable neural recording for up to 3 months. EchoAgent interpreted ultrasound images, planned printing trajectories, generated focused-ultrasound commands, compensated acoustic distortion, and corrected path drift in closed loop.

Together, these components enable a manufacturing logic distinct from conventional implantation. Instead of making an electrode first and forcing it to fit the brain later, AiUP forms the electrode directly where it is needed. We demonstrate pressure-programmable acoustic crosslinking, image-guided in vivo printing, AI-controlled trajectory correction, rodent electrocorticography and epilepsy warning, and large-animal cortical recording and neural decoding in pigs. These results establish AiUP as a minimally invasive acoustic manufacturing paradigm for conformal brain–computer interfaces.

Pressure-programmable ultrasound-responsive inks enable nonthermal acoustic crosslinking

A prerequisite for in-situ ultrasound printing is a material system that responds directly, locally, and safely to ultrasound [30]. Existing ultrasound-assisted manufacturing strategies often depend on heat, cavitation, or indirect physical perturbation. These mechanisms can be difficult to control in neural tissue, where even modest thermal or mechanical damage can impair function[31]. We therefore sought to create a material in which acoustic pressure acts as a programmable mechanochemical instruction rather than as a nonspecific energy input.

We engineered fluorinated silk fibroin hollow nanocages as ultrasound-responsive elements. Silk fibroin was selected because of its biocompatibility, processability, chemical tunability, and capacity to form mechanically robust supramolecular structures. Fluorinated silk fibroin assembled into hollow nanocages through a template-induced self-weaving strategy (Fig. 2a and figs. S1 and S2). Scanning electron microscopy showed intact hollow structures before ultrasound exposure and collapsed structures after activation (Fig. 2b and fig. S3), indicating that focused ultrasound mechanically triggered nanocage failure.

We hypothesized that the acoustic collapse threshold could be programmed by tuning shell mechanics. Because the critical buckling pressure of hollow shells depends on elastic modulus, shell thickness, and geometry, we varied the fluorination degree of silk fibroin (fig. S4 and table S1). This tuning altered the Young's modulus of the nanocage shell (Fig. 2c), changed silk fibroin structure (fig. S5), and shifted the critical acoustic pressure required for collapse (Fig. 2d). Molecular dynamics simulations supported ultrasound-responsive deformation and critical buckling behavior of the nanocages (fig. S6). Crosslinker-loaded nanocages displayed distinct pressure-response profiles, allowing selective release at defined acoustic pressures (Fig. 2e). In mixed populations, increasing ultrasound pressure sequentially activated different nanocage classes with thresholds of approximately 0.4, 1.3, and 2.8 MPa (Fig. 2f). Thus, the nanocages functioned as pressure-programmable mechanochemical switches.

We incorporated these ultrasound-responsive elements into modular ultrasound-printable inks. The ink design included modified polymer chains, pressure-programmable nanocages, conductive modules, therapeutic modules, or imaging components (Fig. 2g and fig. S7). Before ultrasound exposure, the inks remained injectable. After focused-ultrasound activation at physiological temperature, they rapidly transformed into hydrogels (Fig. 2h and fig. S8). Rheological measurements confirmed shear-thinning injectability and ultrasound-triggered gelation (Fig. 2i and j and fig. S9). Increasing acoustic pressure increased the storage modulus, consistent with pressure-dependent nanocage activation and denser crosslinking (Fig. 2d and fig.

S10). Low, intermediate, and high pressures produced weak, double-network, and reinforced hydrogels, respectively (Fig. 2l and fig. S11). Gelation time decreased as pressure increased (Fig. 2m), and kinetic analysis confirmed pressure-sensitive gelation across formulations (Fig. 2n).

The material system supported spatial printing and bioelectronic function. Focused ultrasound generated patterned hydrogels in vitro (Fig. 2o and fig. S12). Cell-viability assays indicated cytocompatibility after printing (Fig. 2p and fig. S13). Thermal monitoring showed limited temperature elevation under printing conditions, supporting a nonthermal mechanism (Fig. 2q and fig. S14). Conductive hydrogels exhibited electrochemical impedance suitable for neural-interface applications (Fig. 2r and fig. S15).

These findings solve a key materials problem for in situ acoustic manufacturing: the absence of directly ultrasound-responsive, pressure-programmable, nonthermally crosslinkable inks. By converting acoustic pressure into localized crosslinker release, the nanocage–ink system allows focused ultrasound to control not only where gelation occurs, but also how the polymer network forms and what mechanical state it reaches. This capability provides the material foundation for soft, conductive, mechanically tunable neural interfaces that can be formed directly on biological surfaces.

Integrated ultrasound imaging–guided printing enables in vivo acoustic manufacturing

After establishing a programmable ink, the next challenge was to deliver acoustic energy precisely in living tissue while monitoring the printing process. Open-loop ultrasound exposure is insufficient because acoustic attenuation, tissue heterogeneity, ink diffusion, and physiological motion continuously alter the relationship between input power and printing outcome. We therefore built an integrated ultrasound imaging–guided focused-ultrasound printing platform.

The system combined focused-ultrasound actuation, high-frequency ultrasound imaging, phased-array control, motorized positioning, image analysis, and feedback regulation (Fig. 3a and fig. S16). A 64-element phased-array transducer generated electronically steered focused ultrasound, whereas high-frequency imaging localized tissue anatomy, ink distribution, focal position, and printing progression (Fig. 3b). Hydrophone measurements and simulations confirmed confined acoustic-pressure fields at the focal zone using a 1.88-MHz transducer (Fig. 3c). Ultrasound imaging tracked the focus at different depths and visualized in vivo printing traces in real time (Fig. 3d and e).

We first evaluated subcutaneous in vivo printing. After minimally invasive ink delivery, focused ultrasound activated gelation only within the focal zone, while ultrasound imaging monitored ink distribution and focus position (Fig. 3f and g). Recovered printed structures retained the designed morphologies (Fig. 3h). In vivo nanocage conversion increased with acoustic pressure, consistent with the programmable release mechanism observed in vitro (Fig. 3i and fig. S17). Mechanical measurements defined the printing window and identified conditions that caused insufficient gelation or structural disruption (Fig. 3j). Acoustic pressure calibration against input power established operating parameters for ultrasound printing (Fig. 3k).

Printing resolution depended on acoustic power, printing speed, frequency, and substrate conditions (Fig. 3l to o and fig. S18 and table S2). Printability maps identified parameter combinations that produced continuous structures in vivo (Fig. 3m). Ex vivo pork and beef substrates confirmed that printing resolution could be tuned under tissue-like acoustic conditions (Fig. 3o and fig. S19). Under acoustic distortion, closed-loop operation maintained higher pattern fidelity than open-loop printing (Fig. 3p and fig. S20). The system printed complex scaffolds,

electrode-like structures, hierarchical catheter-like structures, and strain sensors (Fig. 3q and r and figs. S21 and S22), demonstrating broader soft-bioelectronic printability. Printed US-gels also exhibited ultrasound-regulated degradation (fig. S23), suggesting that acoustic control can extend beyond fabrication to post-printing remodeling or removal.

We then applied the platform to cortical electrode fabrication. Conductive ink was delivered to the dura or cortical surface, and focused ultrasound printed electrode patterns under image guidance (Fig. 3s and figs. S24 and S25). Dissection confirmed printed electrodes on the mouse cerebral cortex, including stimulation electrodes, ultrasound-visible electrodes, and electrocorticography electrodes (Fig. 3t and figs. S26 and S27). Animal survival analysis showed that optimized printing conditions were well tolerated (Fig. 3u). Channel-yield analysis confirmed functional multichannel electrode formation (Fig. 3v), and repeated rat experiments showed high printing success across independent batches (Fig. 3w).

These results transform in vivo ultrasound printing from a blind exposure process into a visible, registered, and feedback-controllable manufacturing operation. The integration of imaging and actuation is critical because in vivo fabrication must adapt to tissue-specific acoustic fields and continuously changing biological conditions. It also provides the physical basis for AI control: adaptive printing requires real-time perception of the printing state and precisely executable acoustic output within a unified system.

EchoAgent provides closed-loop AI control of focused-ultrasound printing

Materials and hardware alone are not sufficient for reliable in vivo electrode fabrication. Biological tissues are dynamic acoustic media. Respiratory motion, heartbeat, cerebrospinal-fluid fluctuation, tissue deformation, ink spreading, and acoustic aberration can shift the focus and change the effective pressure during printing [32]. Manual operation cannot continuously interpret high-dimensional ultrasound images, compensate for acoustic distortion, and correct trajectory drift at the temporal resolution required for complex electrode fabrication [33]. We therefore developed EchoAgent, an AI control center for AiUP.

EchoAgent was designed to close the loop between ultrasound perception and focused-ultrasound actuation. It used a mixture-of-experts feature extractor to obtain multilevel representations from ultrasound images, aligned image features with printing parameters, applied spatiotemporal graph convolutional learning to capture dynamic printing states, and used a Transformer-based architecture to generate executable commands (Fig. 4a). An auxiliary contrastive learning branch improved alignment between ultrasound image states and parameter states (Fig. 4a). The training dataset included printing conditions, ultrasound image states, parameter labels, and outcome metrics (Fig. 4b), and the data pipeline supported spatiotemporal learning from ultrasound-guided printing sequences (Fig. 4d). A control dashboard displayed EchoAgent outputs and real-time printing parameters (Fig. 4d).

EchoAgent accurately predicted printing parameters in zero-shot tests, with predicted values closely matching labeled experimental parameters (Fig. 4e). Receiver operating characteristic analysis showed improved command-level decision performance compared with alternative printing strategies (Fig. 4f). Under perturbations including noise, motion, and acoustic distortion, EchoAgent maintained higher robustness than manual or nonadaptive strategies (Fig. 4g). Compared with manual control, EchoAgent improved printing accuracy, continuity, and structural integrity (Fig. 4h).

Closed-loop experiments showed convergence of printing error during iterative feedback (Fig. 4i). Path-agreement analysis demonstrated improved consistency among designed paths, predicted paths, and printed outcomes (Fig. 4j). Final structures printed under EchoAgent control showed high reproducibility and fidelity (Fig. 4k and l). Mechanistically, EchoAgent predicted target paths, compensated for acoustic-pressure distortion, and corrected focal drift; ultrasound imaging confirmed improved printing outcomes compared with printing without EchoAgent (Fig. 4m).

EchoAgent was then used for in situ cortical-electrode fabrication. The AI controller generated and executed electrode-printing commands, producing conformal electrodes in vivo (Fig. 4n). The closed-loop workflow consisted of ultrasound-image acquisition, target recognition, path planning, pressure compensation, focused-ultrasound execution, feedback imaging, and iterative correction (Fig. 4o). Compared with manual operation, EchoAgent increased printing accuracy, reduced time cost, and improved structural integrity (Fig. 4p).

These results transform in vivo ultrasound printing from a blind exposure process into a visible, registered, and feedback-controllable manufacturing operation. The integration of imaging and actuation is critical because in vivo fabrication must adapt to tissue-specific acoustic fields and continuously changing biological conditions. It also provides the physical basis for AI control: adaptive printing requires real-time perception of the printing state and precisely executable acoustic output within a unified system. This improvement was most pronounced under combined perturbations, indicating that EchoAgent learned coupled image–parameter–outcome relationships that were not captured by rule-based feedback.

AiUP prints conformal cortical electrodes in rodents

We next asked whether AiUP could fabricate functional cortical electrodes in small animals. Rodent brains provide a stringent test because surgical windows are small, cortical surfaces are delicate, and interfacial mismatch strongly affects signal stability. We evaluated whether AiUP could generate conformal electrodes in situ with high channel yield, stable electrophysiology, low artifact susceptibility, and favorable tissue compatibility.

Conductive ink was minimally delivered to the target region and remotely patterned by focused ultrasound into soft electrode arrays (Fig. 5a). EchoAgent localized the ink, mapped the cortical surface, defined focal motion paths, set printing depth, and generated trajectories for recording sites, serpentine interconnects, and connector pads (Fig. 5b). In mice, fluorescence imaging confirmed printed electrode patterns in vivo, ultrasound imaging monitored electrode formation, and dissection verified electrodes on the cortical surface (Fig. 5c). In rats, channels were arranged according to cortical recording targets (Fig. 5d). Resistance measurements showed stable electrical performance after printing (Fig. 5e).

AiUP-printed electrodes recorded spontaneous local field potentials and spike waveforms in rats (Fig. 5f and g). Time-frequency spectrograms showed channel-specific local field potential power (Fig. 5h). Compared with commercial patch electrodes, printed electrodes exhibited improved signal-to-noise ratio (Fig. 5i). Longitudinal measurements demonstrated stable SNR over time (Fig. 5j). During rest and visual stimulation, printed electrodes preserved neural signals with reduced motion artifacts compared with commercial invasive soft electrodes (Fig. 5k and l). These advantages likely arise from the conformal hydrogel interface, mechanical matching, stable hydration, and reduced interfacial slip.

We further evaluated disease-relevant monitoring in a mouse epilepsy model (Fig. 5m). Printed electrodes recorded distinct local field potential patterns during resting and epileptic states, and spectrograms revealed seizure-associated spectral changes (Fig. 5n). Power spectral density analysis distinguished brain states (Fig. 5o). Compared with Ag electrodes, printed electrodes achieved favorable SNR for early epilepsy detection (Fig. 5p and fig. S28). Receiver operating characteristic analysis showed that printed electrodes supported early seizure warning with strong classification performance (Fig. 5q). Multichannel recordings captured resting-state and late epileptic activity, together with corresponding time-frequency features (Fig. 5r and s and fig. S29).

Biosafety evaluation showed preserved neuronal marker expression and limited glial activation after electrode printing, as assessed by NeuN and GFAP staining (Fig. 5t). Together, the rodent experiments demonstrate that AiUP-printed electrodes are functional neural interfaces rather than merely printable structures. By forming electrodes directly on the neural surface, AiUP reduces the need to mechanically position a prefabricated device against delicate tissue. The resulting conformal hydrogel interface provides stable impedance, improved signal-to-noise ratio, reduced motion artifacts, long-term recording stability, biocompatibility, and disease-state detection capability.

AiUP enables large-animal cortical recording and neural decoding in pigs

Large-animal validation is a critical step toward clinical translation of in situ neural-interface manufacturing. Compared with rodents, pigs present a substantially larger brain, more complex cortical geometry, thicker overlying tissues, stronger acoustic attenuation and heterogeneity, and surgical conditions that more closely approximate those encountered in human applications. These features provide a stringent test of whether AiUP can be scaled from small-animal cortical printing to large-animal neuroengineering. We therefore evaluated AiUP in pigs using a stepwise strategy: first, minimally invasive subcutaneous electrode printing was performed to establish the feasibility of acoustic electrode fabrication and EEG recording through large-animal soft tissues; subsequently, AiUP was applied to direct cortical-surface printing to fabricate conformal ECoG arrays for high-fidelity cortical recording and neural decoding.

We first assessed whether AiUP could fabricate functional subcutaneous electrodes in pigs using a minimally invasive workflow. Conductive US-Ink was delivered beneath the skin, localized by ultrasound imaging, and patterned by EchoAgent-guided focused ultrasound to form soft electrodes without mechanical insertion of a prefabricated device (Fig. 6a and fig. S30 and movie S2). This configuration served as an intermediate validation between superficial bioelectronic printing and intracranial cortical-interface fabrication. It tested the ability of AiUP to operate under large-animal acoustic conditions while maintaining the advantages of remote, image-guided, and noncontact manufacturing. Real-time imaging confirmed that electrode formation could be monitored during printing and that the focused-ultrasound focal point could be tracked throughout the process (Fig. 6b and d). Subcutaneously printed electrodes recorded representative EEG signals from pigs under both anesthetized and awake states (Fig. 6e and f). Power spectral density analysis further showed that the printed electrodes captured brain-state-dependent spectral features comparable to those recorded using commercial electrodes (Fig. 6g and h). These results demonstrate that AiUP can fabricate minimally invasive subcutaneous neural electrodes in a large animal and support stable EEG acquisition, highlighting its potential for long-term or reduced-access neural monitoring.

Having established the feasibility of AiUP-based electrode manufacturing in the subcutaneous large-animal setting, we next advanced the strategy to direct cortical-surface fabrication. In this configuration, conductive US-Ink was delivered to the exposed cortical surface and printed into a conformal electrode array under ultrasound-image guidance. The printed cortical electrodes were positioned over porcine somatosensory and visual cortices to enable ECoG recording during sensory and visual stimulation (Fig. 6c and fig. S31). This step represented a more demanding implementation of AiUP because the electrode had to conform to the curved, hydrated, and pulsatile cortical surface while preserving multichannel electrical functionality. Ultrasound imaging visualized electrode formation and focal-point progression during printing, supporting accurate pattern formation under large-animal surgical conditions (Fig. 6d). Together, the subcutaneous and cortical experiments demonstrate that AiUP can be deployed across different anatomical depths and interface configurations, progressing from minimally invasive EEG recording to conformal cortical ECoG fabrication.

Printed 16-channel cortical arrays recorded robust ECoG signals during tibial-nerve electrical stimulation and visual stimulation (Fig. 6i and j). Overlaid segmented recordings revealed channel-dependent response differences across stimulation conditions, indicating spatially resolved cortical sensitivity of the printed arrays (Fig. 6k and l). Time–frequency spectrograms from selected channels over the somatosensory cortex showed stimulation-associated cortical dynamics (Fig. 6m). Cortical surface voltage maps reconstructed from the printed 16-channel array further localized activity over the left sensorimotor cortex (Fig. 6n). Power spectral density analysis confirmed region-specific cortical activation recorded by the printed electrodes (Fig. 6o). In addition to evoked responses, the printed arrays captured tactile-stimulation responses and state-dependent cortical activity under behavioral and light-anesthesia conditions (fig. S32), demonstrating that AiUP-printed cortical interfaces can record both externally evoked and spontaneous large-animal neural activity.

We next examined whether the electrophysiological signals recorded by AiUP-printed cortical electrodes were sufficient for neural decoding. Low-frequency and high-gamma ECoG features were used as inputs to a convolutional recurrent neural network comprising a one-dimensional convolutional layer, bidirectional gated recurrent units, and a fully connected layer (fig. S33A). Decoding performance was evaluated across experimental conditions (fig. S33B), and classification analysis distinguished neural activity associated with different behavioral or stimulation states (fig. S33C). Pre-movement cortical activity supported limb-movement decoding, as shown by the confusion matrix (Fig. 6p). AiUP-printed electrodes achieved decoding performance comparable to implanted commercial electrodes (Fig. 6q). Across three pigs, decoding remained effective despite inter-animal variability in tactile-stimulation quality and the number of stimulation sites (Fig. 6r). Pearson correlation analysis of spontaneous cortical activity as a function of interelectrode distance and ECoG frequency band revealed spatially structured neural correlations recorded by the printed arrays (Fig. 6s), further supporting the physiological relevance of the recorded signals.

Together, these large-animal results establish pigs as a practical and scalable preclinical platform for evaluating AiUP-enabled neural interfaces and neural decoding. Compared with non-human primates, pigs are more widely available, have lower animal and experimental costs, and allow shorter experimental preparation cycles, while still providing a large gyrencephalic brain, clinically relevant cortical dimensions, and surgical conditions that are more representative of human neuroengineering than rodent models. In this context, AiUP first enabled minimally invasive subcutaneous EEG electrode printing for brain-state monitoring and then advanced to

direct cortical ECoG array fabrication for spatially resolved recording and movement-related decoding. This stepwise validation demonstrates that AiUP can manufacture neural interfaces at different anatomical depths and functional levels in a cost- and time-efficient large-animal model. Successful EEG recording, cortical mapping, and neural decoding in pigs therefore not only strengthen the translational potential of AiUP for personalized conformal brain–computer interfaces but also suggest that pig electrophysiology could serve as an accessible alternative to non-human primates for preclinical neural-decoding studies.

Discussion

Brain–computer interfaces have traditionally been engineered as prefabricated devices that are subsequently implanted onto or into neural tissue. This workflow has enabled major advances in cortical recording, neural decoding and neuromodulation, but it also imposes an inherent mismatch between a static device and a soft, curved, hydrated and moving brain surface. Here we establish AI-guided in situ ultrasound printing, termed AiUP, as an alternative manufacturing paradigm in which neural interfaces are formed directly at the site of function. By integrating pressure-programmable ultrasound-responsive nanocages, modular conductive inks, ultrasound imaging–guided focused-ultrasound actuation and closed-loop AI control, AiUP converts focused ultrasound from an energy-delivery modality into a programmable manufacturing tool for conformal bioelectronic interfaces.

A central advance of this study is the conversion of acoustic pressure into a defined mechanochemical instruction. Existing in vivo printing or curing strategies are often constrained by limited light penetration, tissue heating, mechanical contact or insufficient control over deep-tissue patterning. In contrast, the fluorinated silk fibroin hollow nanocages developed here collapse at tunable acoustic-pressure thresholds and release crosslinkers to initiate localized, nonthermal hydrogel formation. This pressure-gated mechanism allows ultrasound to regulate not only the spatial location of gelation but also the network architecture and mechanical state of the printed hydrogel. The resulting conductive US-Inks remain injectable before activation, rapidly gel under focused ultrasound, support electrochemical properties suitable for neural recording and can be further engineered through modular functional components. These features address a key materials bottleneck in in situ bioelectronic manufacturing: the lack of soft, conductive and directly ultrasound-programmable inks that can be transformed safely and locally in living tissue.

The second advance is the integration of imaging and actuation into a single feedback-controllable acoustic manufacturing platform. In vivo printing cannot rely on fixed exposure parameters, because acoustic attenuation, tissue heterogeneity, ink spreading and physiological motion continuously alter the relationship between the commanded acoustic field and the final printed structure. By combining focused-ultrasound actuation with real-time ultrasound imaging, AiUP registers tissue anatomy, ink distribution, focal position and structure formation during fabrication. This capability distinguishes AiUP from open-loop sound-printing approaches and is particularly important for neural interfaces, where small deviations in electrode location, continuity or contact can compromise recording stability. The system achieved rapid gelation, microscale-to-submillimetre patterning, reproducible in vivo printing and functional multichannel electrode formation on the dura or cortical surface, demonstrating that acoustic manufacturing can be adapted to the constraints of living neural tissue.

A third innovation is EchoAgent, which provides closed-loop AI control over the printing process. Biological tissues act as dynamic acoustic media, and manual operation is poorly suited

to continuously compensate for motion, acoustic aberration and path drift. EchoAgent links ultrasound image perception to executable focused-ultrasound commands through spatiotemporal learning, trajectory planning and pressure compensation. Its improved performance under combined perturbations indicates that it captures coupled image–parameter–outcome relationships beyond simple rule-based feedback. This capability is important not only for improving printing fidelity but also for establishing a scalable route toward patient-specific fabrication, where anatomy, acoustic windows and target geometries vary across individuals.

The functional data show that AiUP-printed structures are not merely printable hydrogels but operational neural interfaces. In rodents, in situ printed electrocorticography electrodes recorded spontaneous local field potentials and spike-like activity, showed stable impedance and signal-to-noise ratio, reduced motion artifacts relative to commercial electrodes and enabled early seizure-warning analysis. The preservation of neuronal marker expression and limited glial activation further support the biocompatibility of the optimized printing conditions. These results are consistent with the design principle that a conformal hydrogel interface, formed directly on the neural surface, reduces interfacial slip and mechanical mismatch compared with prefabricated devices that must be mechanically positioned after fabrication.

Large-animal experiments further support the scalability of AiUP. In pigs, AiUP fabricated subcutaneous electrodes that recorded brain-state-dependent EEG signals and cortical electrode arrays that captured sensory, visual, tactile, anaesthesia-state-dependent and movement-related activity. The printed 16-channel cortical arrays resolved spatially structured cortical responses and supported neural decoding with performance comparable to implanted commercial electrodes. These results are significant because pigs provide a large gyrencephalic brain, clinically relevant cortical dimensions and surgical conditions that are closer to human neuroengineering than rodent models. The stepwise validation from subcutaneous EEG recording to direct cortical ECoG fabrication suggests that AiUP can operate across different anatomical depths and interface configurations. It also indicates that pig electrophysiology may provide an accessible preclinical platform for evaluating in situ manufactured neural interfaces and neural-decoding algorithms before studies in non-human primates or humans.

Several limitations remain. First, the present cortical-printing demonstrations required local ink delivery and, for direct cortical ECoG fabrication, surgical access to the dura or brain surface. Fully transcranial or closed-skull printing will require more advanced skull-aberration correction, individualized acoustic modelling and safe strategies for targeted ink delivery. Second, although the electrodes showed stable recording for months in rodents, chronic large-animal studies are needed to assess long-term material stability, immune response, degradation, adhesion, impedance drift and functional reliability under clinically relevant motion and behavioural conditions. Third, future devices will require higher-density arrays, improved interconnect architectures, stimulation capability, wireless data transmission and integration with implantable electronics. Finally, translation will require regulatory-grade characterization of the ink components, acoustic exposure limits, degradation products, sterilization procedures and manufacturing reproducibility.

Despite these challenges, AiUP changes the design logic of neural interfaces. Rather than fabricating electrodes as finished objects and forcing them to fit the brain during surgery, AiUP manufactures soft conductive interfaces in situ according to local anatomy, tissue mechanics and functional demand. This shift may reduce mechanical manipulation, improve conformity and enable personalized electrode geometries that are difficult to achieve with prefabricated arrays. More broadly, the platform suggests a route toward bioelectronic systems that are acoustically

written, remodelled or removed within living tissues when and where they are needed. By coupling programmable materials, real-time imaging and adaptive AI control, AiUP provides a foundation for next-generation conformal brain–computer interfaces and for in situ acoustic manufacturing of soft bioelectronics beyond the nervous system.

References

1. Bae, J.-Y. *et al.*, A biodegradable and self-deployable electronic tent electrode for brain cortex interfacing. *Nat. Electron.* **7**, 815-828 (2024).
2. Coles, L. *et al.*, Origami-inspired soft fluidic actuation for minimally invasive large-area electrocorticography. *Nat. Commun.* **15**, 6290 (2024).
3. Fang, R. *et al.*, Flexible kirigami microelectrode arrays for neuronal activity recordings in non-human primate brains. *Nat. Electron.* **9**, 266-278 (2026).
4. Hettick, M. *et al.*, minimally invasive implantation of scalable high-density cortical microelectrode arrays for multimodal neural decoding and stimulation. *Nat. Biomed. Eng.* **10**, 1206-1221 (2026).
5. Jung, T. *et al.*, A wireless subdural-contained brain–computer interface with 65,536 electrodes and 1,024 channels. *Nat. Electron.* **8**, 1272-1288 (2025).
6. Lee, J. M. *et al.*, the ultra-thin, minimally invasive surface electrode array NeuroWeb for probing neural activity. *Nat. Commun.* **14**, (2023).
7. Lee, J. Y. *et al.*, Foldable three-dimensional neural electrode arrays for simultaneous brain interfacing of cortical surface and intracortical multilayers. *NPJ Flex. Electron.* **6**, (2022).
8. Montazerian, H. *et al.*, Boosting hydrogel conductivity via water-dispersible conducting polymers for injectable bioelectronics. *Nat. Commun.* **16**, 3755 (2025).
9. Zeng, M. *et al.*, Dopamine-integrated all-hydrogel multi-electrode arrays for neural activity recording. *Mater. Horiz.* **11**, 6423-6434 (2024).
10. Wang, Z. *et al.*, Tissue-specific engineering: 3D bioprinting in regenerative medicine. *J. Control. Release* **329**, 237-256 (2021).
11. Yang, X. *et al.*, Kirigami electronics for long-term electrophysiological recording of human neural organoids and assembloids. *Nat. Biotechnol.* **42**, 1836-1843 (2024).
12. Cui, Y. *et al.*, A Stretchable and Transparent Electrode Based on PEGylated Silk Fibroin for In Vivo Dual-Modal Neural-Vascular Activity Probing. *Adv. Mater.* **33**, e2100221 (2021).
13. Cadena, M. *et al.*, 3D Bioprinting of Neural Tissues. *Adv. Healthc. Mater.* **10**, e2001600 (2021).
14. Gupta, D. *et al*., Ozbolat, Droplet-based bioprinting. *Nat. Rev. Method. Prime.* **5**, (2025).
15. P. Le Floch *et al.*, 3D spatiotemporally scalable in vivo neural probes based on fluorinated elastomers. *Nat. Nanotechnol.* **19**, 319-329 (2024).
16. E. Davoodi *et al*., Imaging-guided deep tissue in vivo sound printing. *Science* **388**, 616-623 (2025).
17. You, S. *et al*., High cell density and high-resolution 3D bioprinting for fabricating vascularized tissues. *Sci. Adv.* **9**, eade7923 (2023).
18. Zhang, S. *et al.*, In Situ Endothelialization of Free-Form 3D Network of Interconnected Tubular Channels via Interfacial Coacervation by Aqueous-in-Aqueous Embedded Bioprinting. *Adv. Mater.* **35**, e2209263 (2023).
19. Sun, Y. *et al*., 3D bioprinting dual-factor releasing and gradient-structured constructs ready to implant for anisotropic cartilage regeneration. *Sci. Adv.* **6**, eaay1422 (2020).
20. Shiwarski, D. J. *et al*. ,3D bioprinting of collagen-based high-resolution internally perfusable scaffolds for engineering fully biologic tissue systems. *Sci. Adv.* **11**, eadu5905 (2025).

21. Tay, R. Y. *et al*., Direct-Ink-Writing 3D-Printed Bioelectronics. *Mater. Today (Kidlington)* **71**, 135-151 (2023).
22. Zhang, Y. *et al*., Regenerative cell therapy with 3D bioprinting. *Science* **385**, 604-606 (2024).
23. Chen, S. *et al.*, Wearable Ultrasound Devices for Therapeutic Applications. *Nanomicro. Lett.* **18**, 45 (2025).
24. Yao, G. *et al.*, Sound Continuous Production of Thermosets. *Adv. Funct. Mater.* **34**, (2023).
25. Habibi, M. *et al*., Direct sound printing. *Nat. Commun.* **13**, (2022).
26. Debbi, L. *et al.*, Ultrasound Mediated Polymerization for Cell Delivery, Drug Delivery, and 3D Printing. *Small Methods* **8**, e2301197 (2024).
27. Gou, S. *et al.*, Non-Pore Dependent and MMP-9 Responsive Gelatin/Silk Fibroin Composite Microparticles as Universal Delivery Platform for Inhaled Treatment of Lung Cancer. *Adv. Mater.* **35**, (2023).
28. Gou, S. *et al.*, Glutathione-Responsive and Hydrogen Sulfide Self-Generating Nanocages Based on Self-Weaving Technology to Optimize Cancer Immunotherapy. *ACS Nano* **18**, 9871-9885 (2024).
29. Li, M. *et al.*, clinically translatable ultrasound localization microscopy reveals cerebrovascular remodelling and prognosis in patients with traumatic brain injury. *Nat. Biomed. Eng*. (2026).
30. Kuang, X. *et al.*, Sonicated inks and focused ultrasound writing enable deep-penetration acoustic volumetric printing. *Nat. Protoc.* **21**, 2919-2959 (2026).
31. Foroughi, S. *et al*, Proximal sound printing: direct 3D printing of microstructures on polymers. *Microsyst. Nanoeng.* **12**, 12 (2026).
32. Yu, M. *et al.*, A Conformal Wearable Ultrasound Bioelectronics for Mechanotherapy Reprogramming of Fibroblast Plasticity via Wnt-FGF10 Axis to Overcome Fibrotic Healing in Urethral Regeneration. *Adv. Sci. (Weinh)* **13**, e00037 (2026).
33. Zhou, J. *et al.*, A non-invasive end-to-end intelligent assistance system for breast ultrasound. *Nat. Commun*. **13**, 7301 (2026).

Methods

Preparation of ultrasound-responsive elements (UREs)

Preparation of regenerated silk fibroin

Regenerated silk fibroin (RSF) was prepared according to a standard degumming and dissolution protocol. Briefly, silk cocoons were boiled in sodium carbonate solution to remove sericin, thoroughly rinsed with deionized water, and dried. The degummed silk fibers were dissolved in lithium bromide solution and dialyzed against deionized water to remove residual salts. The resulting RSF solution was clarified by centrifugation and lyophilized for subsequent modification.

Synthesis of fluorinated silk fibroin (FSF)

Lyophilized RSF was dissolved in deionized water to obtain a 3 wt.% solution and hydrated overnight at 4 °C. Heptafluorobutyric anhydride was dissolved in DMSO at a concentration of 10 mg/mL. The heptafluorobutyric anhydride solution was then added dropwise to the RSF solution at a volume ratio of 1:5 under vigorous stirring. The mixture was vortexed for 2 min, and the pH was maintained at 8.0 by the real-time addition of 1 M NaOH. After reaction for 6 h at room temperature, the mixture was stored at 4 °C overnight. The reaction solution was transferred into dialysis tubing and dialyzed against distilled water for 3 days at room temperature, with frequent

water changes. The purified fluorinated silk fibroin (FSF) was collected by lyophilization and stored at −20 °C until use.

Fabrication of FSF-based nanocages

Sodium carbonate nanoparticles were prepared as sacrificial templates and dispersed in deionized water at a concentration of 0.5 mg/mL by sonication and vortexing. The FSF microemulsion was added dropwise to the template suspension at a volume ratio of 1:5. The mixture was vigorously vortexed until phase separation occurred. The upper oil phase was discarded, and the lower milky emulsion was further vortexed in an ice bath for 10 min. The FSF-based nanocages were collected by centrifugation at 11,000 rpm for 20 min, washed three times with deionized water, and stored at −20 °C. To remove the sacrificial templates and stabilize the cage structure, the nanocages were resuspended in phosphate-buffered saline (PBS, pH 5.0) containing an appropriate crosslinking agent at a final nanocage concentration of 2 wt.%. The suspension was stirred at 4 °C for 2 h. The etched nanocages were then collected by centrifugation at 11,000 rpm for 20 min, washed three times with deionized water to remove residual ions and reagents, lyophilized, and stored at −20 °C until further use.

Dopamine modification of nanocages

Lyophilized nanocages were resuspended in deionized water at a concentration of 1 wt.%. An EDC/NHS activation solution was prepared at a total concentration of 5 mg/mL with an EDC: NHS mass ratio of 1:1. The nanocage suspension was mixed with an equal volume of EDC/NHS solution and stirred at room temperature for 6 h to activate surface carboxyl groups. Dopamine hydrochloride was then added at a concentration of 2 mg per reaction batch, and the mixture was vigorously vortexed for 2 min. The pH was maintained at 6.0 by the addition of hydrochloric acid. After reaction for 6 h, the mixture was incubated at 4 °C overnight. The product was dialyzed against distilled water for 3 days at room temperature and lyophilized to obtain dopamine-modified ultrasound-responsive elements, hereafter referred to as UREs.

Characterization of UREs

The morphology of UREs before and after focused ultrasound exposure was characterized by transmission electron microscopy (TEM) and scanning electron microscopy (SEM). The hydrodynamic diameter and size distribution were measured by dynamic light scattering. The acoustic response threshold was determined by exposing URE suspensions to defined acoustic pressures and quantifying the collapse fraction using microscopy, light scattering, and/or release-based assays. URE formulations with distinct activation thresholds were designated URE-1, URE-2, and URE-3 and were used for selective ultrasound-triggered crosslinking.

Preparation of modular ultrasound-printable ink (US-Ink)

Synthesis of Thiol- and Azide-modified hyaluronic acid

Hyaluronic acid was dissolved in deionized water at a concentration of 10 wt.%. An EDC/NHS activation solution was prepared in deionized water at a total concentration of 10 mg/mL with an EDC: NHS mass ratio of 1:1. Equal volumes of HA solution and EDC/NHS solution were mixed and stirred at room temperature for 6 h to activate carboxyl groups on HA. Subsequently, NH_2-PEG-SH and NH_2-PEG-N_3 were added to the activated HA solution. The mixture was vortexed for 2 min, and the pH was maintained at 6.0 by the addition of hydrochloric acid. The reaction was allowed to proceed for at least 6 h and then incubated at 4 °C overnight. The reaction mixture was dialyzed against distilled water for 3 days at room temperature and lyophilized to obtain thiol- and azide-functionalized hyaluronic acid, designated SH-HA-N_3.

Synthesis of Thiolated poly-L-lysine

COOH-PEG-SH was dissolved in deionized water at a concentration of 5 mg/mL. An EDC/NHS solution with the same formulation described above was mixed with an equal volume of COOH-

PEG-SH solution and stirred at room temperature for 6 h to activate the carboxyl groups. The activated COOH-PEG-SH solution was then added to a 5 wt.% aqueous PLL solution at an equal volume ratio. After vigorous vortexing for 2 min, the pH was adjusted to and maintained at 6.0 using hydrochloric acid. The reaction proceeded for 6 h at room temperature, followed by incubation at 4 °C overnight. The solution was dialyzed against distilled water for 3 days and lyophilized to obtain thiolated poly-L-lysine, designated SH-PLL.

Formation of injectable ultrasound-printable Ink

The ultrasound-printable hydrogel precursor, referred to as US-Ink, was prepared by combining SH-HA-N_3, SH-PLL, and UREs. Briefly, 2 wt.% SH-HA-N_3 was mixed with 5 wt.% SH-PLL to form a hydrogel precursor matrix. The mixture was degassed under vacuum to remove trapped air bubbles. URE-1, URE-2, and URE-3 were then incorporated into the precursor matrix by physical blending to obtain a biosafe, acoustic responsive ink. The loading concentration of each URE formulation and the blending strategy were optimized according to subsequent rheological characterization, gelation behavior, and analysis of the ultrasound-triggered crosslinking mechanism.

For functional applications, additional components were incorporated into US-Ink as required. To prepare conductive ultrasound-printable bioinks, conductive additives, including PEDOT: PSS, graphene, carbon nanotubes, silver nanowires, or MXene, were added to the ink formulation. Unless otherwise specified, the conductive additive concentration was 5 wt.%. To further enhance conductivity, 0.2 wt.% of silver nanowires were incorporated into carbon nanotube-containing US-Ink. For improved visualization during printing, 0.2 wt.% oil-soluble dye was added to the base precursor formulation.

Rheological characterization of US-Ink

Rheological properties were measured using a rotational rheometer. Shear-rate-dependent viscosity was recorded to evaluate injectability and shear-thinning behavior. Time-sweep rheological measurements were performed during or immediately after ultrasound exposure to determine gelation kinetics. Storage modulus and loss modulus were monitored as functions of time. The final mechanical properties of the printed gels were measured under different acoustic pressures and URE compositions to determine the relationship between ultrasound activation, crosslinking density, and gel stiffness.

Materials characterizations

Raman spectroscopy was performed using a inVia Raman microscope (Renishaw, UK) to analyze the fluorination degree of silk fibroin, structural changes in silk fibroin before and after fluorination, and chemical or conformational changes in PEDOT chains after phase separation. Atomic force microscopy (AFM; Dimension Icon, Bruker, Germany) was used to characterize phase separation in PEDOT: PSS-based formulations.

Morphological characterizations

SEM (S-4800, Hitachi, Japan) was used to characterize the morphology of UREs, as well as the surface and cross-sectional morphology of printed US-Gels and functional material-doped US-Gels. Samples were freeze-dried, mounted on conductive adhesive tape, and sputter-coated with a thin layer of gold or platinum before imaging when required. TEM (JEM-2100F, JEOL, Japan) was used to examine the hollow structure and nanoscale morphology of UREs.

Mechanical characterizations

For tensile testing, US-Gel samples were printed into rectangular specimens with a thickness of approximately 200 μm. Tensile properties were measured using a dynamic mechanical analyzer

(DMA Q800, TA Instruments, USA) at an extension speed of 20 mm/min. At least five independent specimens were tested for each group. Stress–strain curves were recorded, and tensile strength, elongation at break, and Young's modulus were calculated where appropriate.

Electrical characterizations

The conductivity of printed electrodes was measured using a four-point probe method with a semiconductor analyzer system (ST2742B, Lattice Electronics, China). The inter-probe spacing was 1 mm. Electrical conductivity, σ, was calculated according to:

$$\sigma = 12\pi S(V/I)$$

where S is the inter-probe spacing, V is the potential difference between the second and third probes, and I is the current applied through the first and fourth probes. At least five measurements were performed for each sample, and the average value was reported.

Cyclic voltammetry (CV) of PEDOT: PSS-doped US-Gel electrodes was performed using an electrochemical workstation (Reference 600, Gamry Instruments, USA). An Ag/AgCl electrode was used as the reference electrode, and PBS was used as the electrolyte. Electrochemical properties were analyzed to evaluate charge storage capacity and electrode–electrolyte interface behavior.

In vitro and in vivo biocompatibility evaluation

For in vitro biocompatibility assessment, printed US-Gel samples were placed in 24-well plates and sterilized before cell seeding. PC12 cells were seeded onto the samples at a density of 10,000 cells per well and cultured under standard conditions. Cell viability was evaluated using live/dead staining and observed with a confocal laser scanning microscope (CLSM; Leica TCS SP5, Germany).

For in vivo biocompatibility evaluation, neural electrodes were printed in situ on the dura of rats using the acoustic in vivo ultrasound printing platform. At 7 and 14 days after printing, rats were euthanized, and brain tissues were collected, fixed, sectioned, and stained. Brain sections were stained with DAPI to label nuclei, neurofilament protein (NF) to assess neuronal structures, and glial fibrillary acidic protein (GFAP) to evaluate astrocytic activation and foreign-body response.

Assembly of the ultrasound in vivo printing platform

An integrated acoustic in vivo ultrasound printing platform was constructed to operate with the UREs and modular US-Ink. The core acoustic module consisted of an integrated 64-element ultrasonic transducer array operating at selected frequencies, including 1.88, 2.65, 6.86, and 8.75 MHz. The transducer array comprised 32 elements for focused ultrasound-mediated printing and 32 elements for high-frequency ultrasound imaging. This integrated configuration was designed to enable ultrasound imaging-guided in vivo printing with closed-loop control. This frequency range was selected to match the ultrasound-responsive characteristics and activation thresholds of different URE formulations, enabling selective acoustic triggering and spatially controlled gelation.

To calibrate the focal region of the ultrasound field and ensure accurate energy deposition within URE-containing US-Ink, the transducer was initially excited using short electrical pulses generated by a Panametrics 5072PR pulser/receiver. Received signals were monitored using an oscilloscope (DS1054, Rigol, China), and the focal position was determined by signal analysis. The transducer was mounted on a motorized three-dimensional positioning system capable of high-precision movement with adjustable translation speed. This configuration was designed to accommodate the shear-thinning properties of US-Ink and to support minimally invasive delivery. The positioning platform enabled the transducer to follow predefined trajectories and

generate complex three-dimensional printing patterns. The translation speed was matched to the ultrasound-induced crosslinking rate of the ink to avoid incomplete construction at excessive speeds or material diffusion during overly slow scanning.

The transducer was driven by a function generator (AFG3252, Tektronix, Beaverton, OR USA). The generated waveform was amplified using a radiofrequency power amplifier (A075, Electronics & Innovation, Rochester, NY, USA) and transmitted to the transducer. Output power was monitored in real time using the amplifier display. The power adjustment range was selected to match the critical acoustic pressure thresholds of different UREs, including approximately 0.4, 1.3, and 2.8 MPa, thereby enabling selective activation of distinct URE populations. For high-frequency operation, an impedance-matching network was connected between the radiofrequency amplifier and the focused ultrasound transducer to improve signal transmission efficiency and power stability.

Motion control was implemented using G-code instructions. During printing, the transducer moved along preprogrammed trajectories while ultrasound exposure was synchronized with the printing sequence. Key parameters, including ultrasound power, focal position, acoustic pressure, and transducer translation speed, were preset or adjusted programmatically in real time to match URE activation thresholds and US-Ink gelation kinetics. This platform enabled accurate in situ three-dimensional printing within tissue-mimicking environments and deep biological tissues.

Cortical electrode printing and electrocorticography recording in rat

For rat cortical electrode printing, US-Ink was delivered near the dura or cortical surface through minimally invasive access. Focused ultrasound was applied under ultrasound imaging guidance to trigger localized gelation and fabricate electrode arrays in situ. The printed neural electrode arrays were connected to external acquisition systems for electrophysiological recording.

The AiUP printing parameters for rat experiments were as follows: focused ultrasound frequency, 1.88 MHz; acoustic power, 5 W; acoustic pressure range, 2.8–3.2 MPa; printing speed, 0.3 mm/min; and water bath temperature, 37 °C. The printing probe was controlled using G-code instructions to fabricate an eight-channel bioelectrode array.

Electrocorticography signals were recorded using a multichannel neural signal acquisition system (Blackrock Microsystems/CerePlex, USA). Signals were sampled at 1 kS/s for local field potential recording and filtered using appropriate band-pass settings. In the original acquisition configuration, local field potentials were filtered at 0.5–200 Hz, whereas high-frequency neural activity was recorded using a higher-frequency filtering range when applicable. Raw signals were analyzed in MATLAB. Signal-to-noise ratio was calculated as the ratio of signal power during neural activity or stimulation response to baseline noise power. Epileptic activity prediction was evaluated using pre-ictal signal features and receiver operating characteristic analysis.

ECoG signal detection and analysis

ECoG signals in mouse and rat models were acquired using a multichannel neural signal recording system (Blackrock Microsystems/CerePlex, USA). The neural electrodes were printed in situ by AiUP as described above. The sampling rate was set to 1 kS/s unless otherwise specified. Signals were band-pass filtered at 0.5–500 Hz for local field potential analysis. High-frequency activity was filtered using appropriate frequency bands according to the recording target. Raw ECoG data were further processed using MATLAB. Noise removal, baseline correction, event detection, time–frequency analysis, and signal-to-noise ratio calculations were performed as required.

Validation of AiUP in Bama pig model

Barma minipigs were used to evaluate the feasibility and translational potential of AiUP in a large-animal model. Animals were divided into three groups: an AiUP-printed electrode group, a commercial Ag/AgCl electrode implantation group, and a flexible semi-invasive electrode implantation group. Commercial rigid Ag/AgCl electrodes and flexible semi-invasive electrodes were used as controls to benchmark the performance, conformability, signal quality, and tissue compatibility of printed US-Gel electrodes.

For minipig experiments, AiUP printing parameters were set as follows: focused ultrasound frequency, 1.88 MHz; acoustic power, 8 W; acoustic pressure range, 2.8–3.2 MPa; printing speed, 0.5 cm/min; and water bath temperature, 37 °C. The integrated ultrasound transducer array was controlled using EchoAgent for closed-loop fabrication of a 16-channel bioelectrode array. Electrophysiological signals were acquired using a multichannel neural recording system (Blackrock Microsystems/CerePlex, USA). Recorded signals were processed in MATLAB using appropriate filtering to remove low-frequency drift, power-line interference, and high-frequency noise.

EchoAgent development and evaluation

EchoAgent was developed as a closed-loop control framework for image-guided acoustic printing. The model was trained using multimodal datasets consisting of ultrasound images, acoustic field maps, printing parameters, material states, and experimentally observed printing outcomes.

EchoAgent was developed in three stages. In Stage I, the model performed general ultrasound image feature extraction, including tissue boundary recognition, target localization, and acoustic window assessment. In Stage II, extracted image features were mapped to acoustic and spatial control parameters, including focal depth, acoustic pressure, printing speed, exposure duration, and trajectory correction. In Stage III, executable printing commands were generated using a planning module, tool executor, specialist library, and state cache. These modules enabled iterative updating of printing parameters based on real-time imaging and predicted material responses.

Model performance was evaluated using prediction error, area under the receiver operating characteristic curve, robustness tests, ablation studies, and printing-path agreement between planned and executed trajectories. Printing outcomes were further assessed by comparing target geometry, structural integrity, and functional performance of the printed constructs.

Acknowledgments: We thank the Shenzhen Institutes of Advanced Technology, Chinese Academy of Sciences, for support with TEM and SEM imaging and for computational and technical assistance in EchoAgent development and training. We also thank members of the animal facility, ultrasound imaging, electrophysiology, and data-analysis teams for technical support. AI-assisted tools were used only for language editing; all scientific content, data interpretation, and conclusions were generated and verified by the authors.

Funding:

CZL discloses support for the research of this work from Key Lab of Longgang district (2025BD0001), Shenzhen Peacock Team (KQTD20240729102029016), Research Fund for International Senior Scientists (RFIS- III) of NSFC (W2531016), Shenzhen Medical Research Fund (D250402001). CJ discloses support for publication of this work form the General Program of National Natural Science Foundation of China (82471500), General program

of Guang Dong Basic and Applied Basic Research Foundation (2024A515012060, 2022A1515110206), Peng cheng Peacok Research Fund (2024TC0150, KQ002573), University Development Fund (UDF01002573).

Author contributions:

Conceptualization: SQG, CJ, CZL

Methodology: SQG, PKM., YFW, CHL, WLL, RL

Investigation: SQG, PKM, CHL, CH, AYW, JDZ, LFM, RY, LFM, HL

Visualization: SQG, MPK, WBL, CJ

Funding acquisition: CJ, SQG, YFW, CZL

Project administration: SQG, LCZ

Supervision: WBL, JDZ, CJ, CZL

Writing – original draft: SQG, PKM, CHL

Writing – review & editing: SQG, PKM, CJ, CZL

Competing interests: CZL, SQG, CJ, LM. are inventors on a patent related to ultrasound-responsive modular acoustic printing inks, printing platforms, and applications. The remaining authors declare no competing interests.

Data, code, and materials availability: All data needed to evaluate the conclusions in this paper are present in the paper or the Supplementary Materials. Additional raw data is available from the corresponding author upon reasonable request. Custom code used for EchoAgent training and analysis is available from the corresponding author upon reasonable request.

Supplementary Materials

Materials and Methods

Supplementary Text

Figs. S1 to S33

Tables S1 to S2

Movies S1 to S2

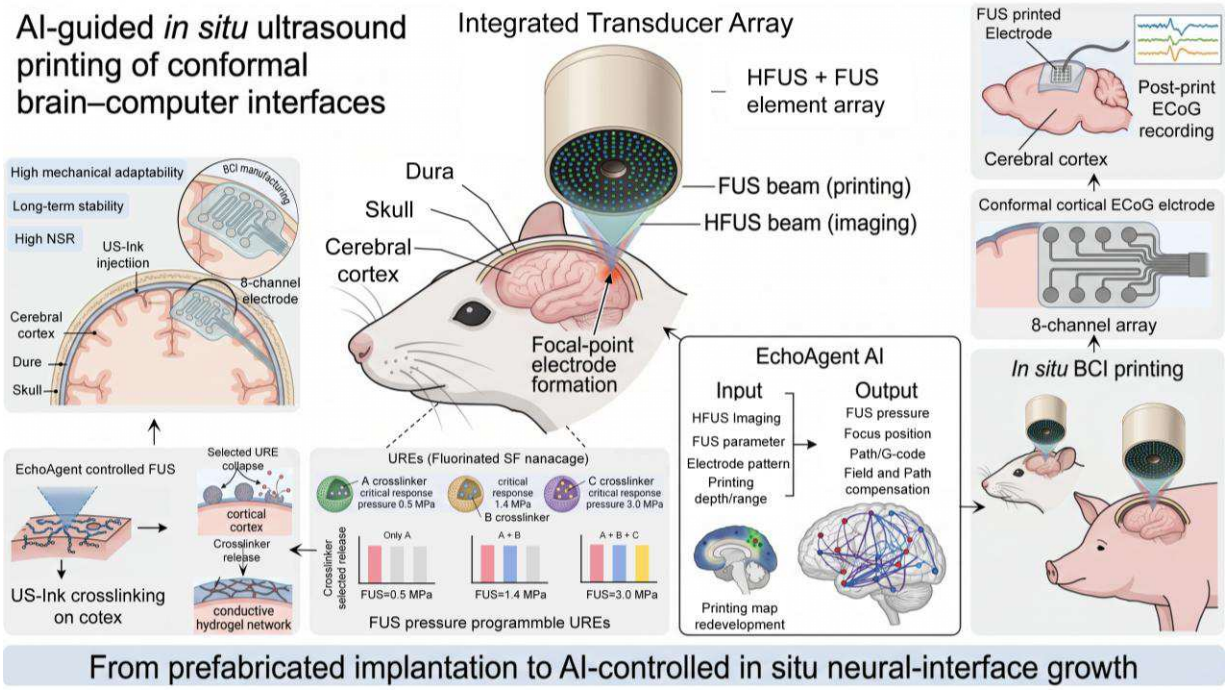


Fig. 1. AI-guided in situ ultrasound printing (AiUP) enables minimally invasive manufacturing of conformal brain–computer interfaces. AI-guided in situ ultrasound printing, termed AiUP, integrates pressure-programmable ultrasound-responsive elements, modular conductive ultrasound-printable inks, ultrasound imaging–guided focused-ultrasound hardware, and the EchoAgent AI controller to fabricate conformal cortical electrodes directly on the dura or brain surface. Fluorinated silk fibroin hollow nanocages collapse at defined acoustic-pressure thresholds to release crosslinkers and trigger localized, nonthermal hydrogel formation. After minimally invasive ink delivery, EchoAgent interprets ultrasound images, plans printing paths, compensates acoustic distortion, and generates executable focused-ultrasound commands. Focused ultrasound selectively activates nanocages at the acoustic focus, forming conductive hydrogel electrode patterns on the cortical surface. AiUP replaces prefabricated neural-interface implantation with AI-controlled, in situ acoustic manufacturing of soft, conformal neural interfaces.

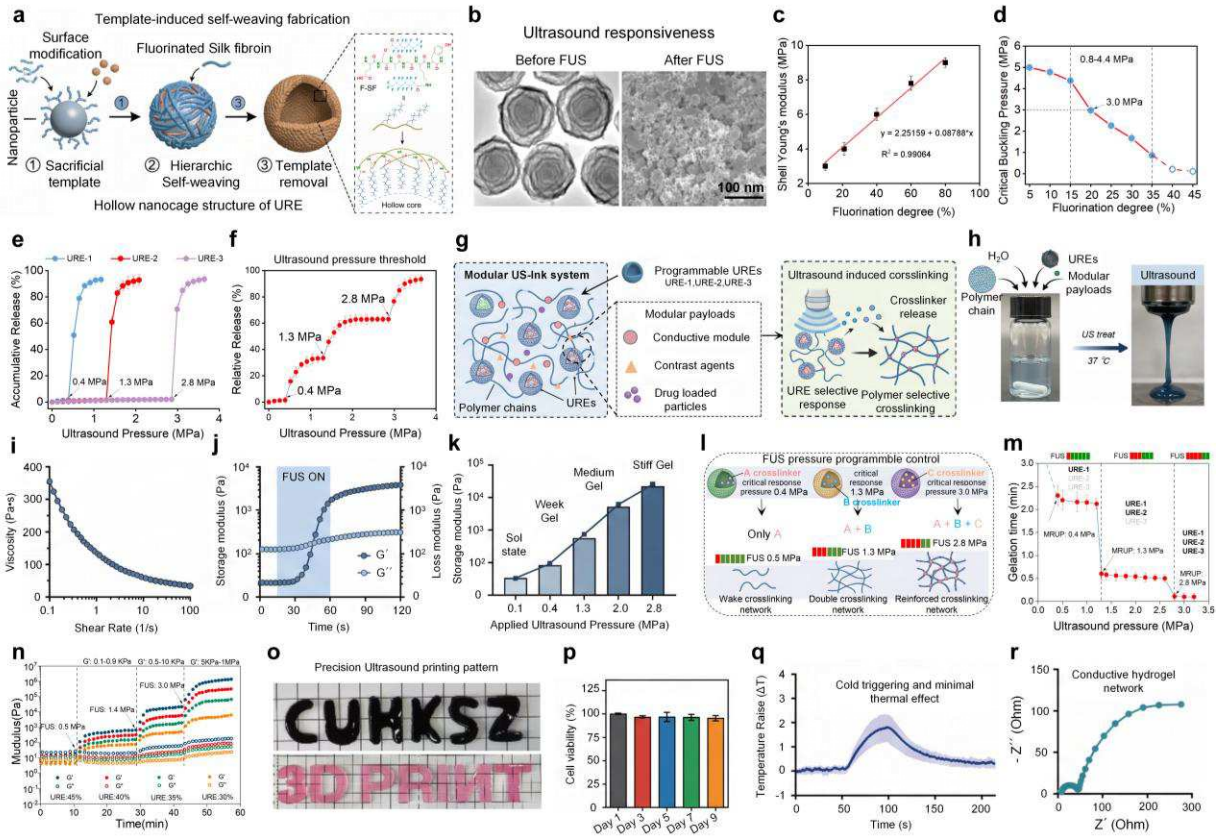


Fig. 2. Pressure-programmable ultrasound-responsive elements and modular US-Ink enable nonthermal acoustic crosslinking. a, Schematic of fluorinated silk fibroin synthesis and fabrication of ultrasound-responsive elements using template-induced self-weaving. **b**, Scanning electron microscopy images of intact and ultrasound-collapsed ultrasound-responsive elements. **c**, Relationship between fluorination degree and Young's modulus of the nanocage shell. **d**, Critical buckling pressure of ultrasound-responsive elements with different fluorination degrees. **e**, Crosslinker release profiles of URE-1, URE-2, and URE-3 under increasing ultrasound pressure, showing distinct pressure-response thresholds. **f**, Selective release of crosslinkers from mixed URE populations under different ultrasound pressures. The critical buckling pressures of URE-1, URE-2, and URE-3 were approximately 0.4, 1.3, and 2.8 MPa, respectively. **g**, Schematic of modular US-Ink composition and ultrasound-triggered crosslinking. Plug-and-play functional modules provide conductivity, drug loading, imaging contrast, or other functions without disrupting the pressure-programmable acoustic response of the ink. **h**, Photographs of US-Ink before and after ultrasound-induced gelation at 37°C. **i**, Viscosity of US-Ink as a function of shear rate. **j**, Rheological measurement of storage modulus and loss modulus before and after focused-ultrasound activation. **k**, Storage modulus of US-gels formed under different ultrasound pressures. **l**, Schematic of pressure-programmable crosslinking networks. Activation of one crosslinker produces a weakly crosslinked network, activation of two crosslinkers produces a double network, and activation of three crosslinkers produces a reinforced network. **m**, Gelation time of US-Ink under different ultrasound pressures. **n**, Gelation kinetics of US-Inks containing different URE contents under focused-ultrasound treatment. **o**, in vitro focused-ultrasound–printed US-gel pattern. Scale bar, 1 cm. **p**, Cytocompatibility of focused-ultrasound–printed US-

gel patterns. **q**, Temperature changes at the acoustic focal point during US-Ink printing. **r**, Electrochemical impedance spectroscopy of printed conductive hydrogels. Data are shown as mean ± s.d.

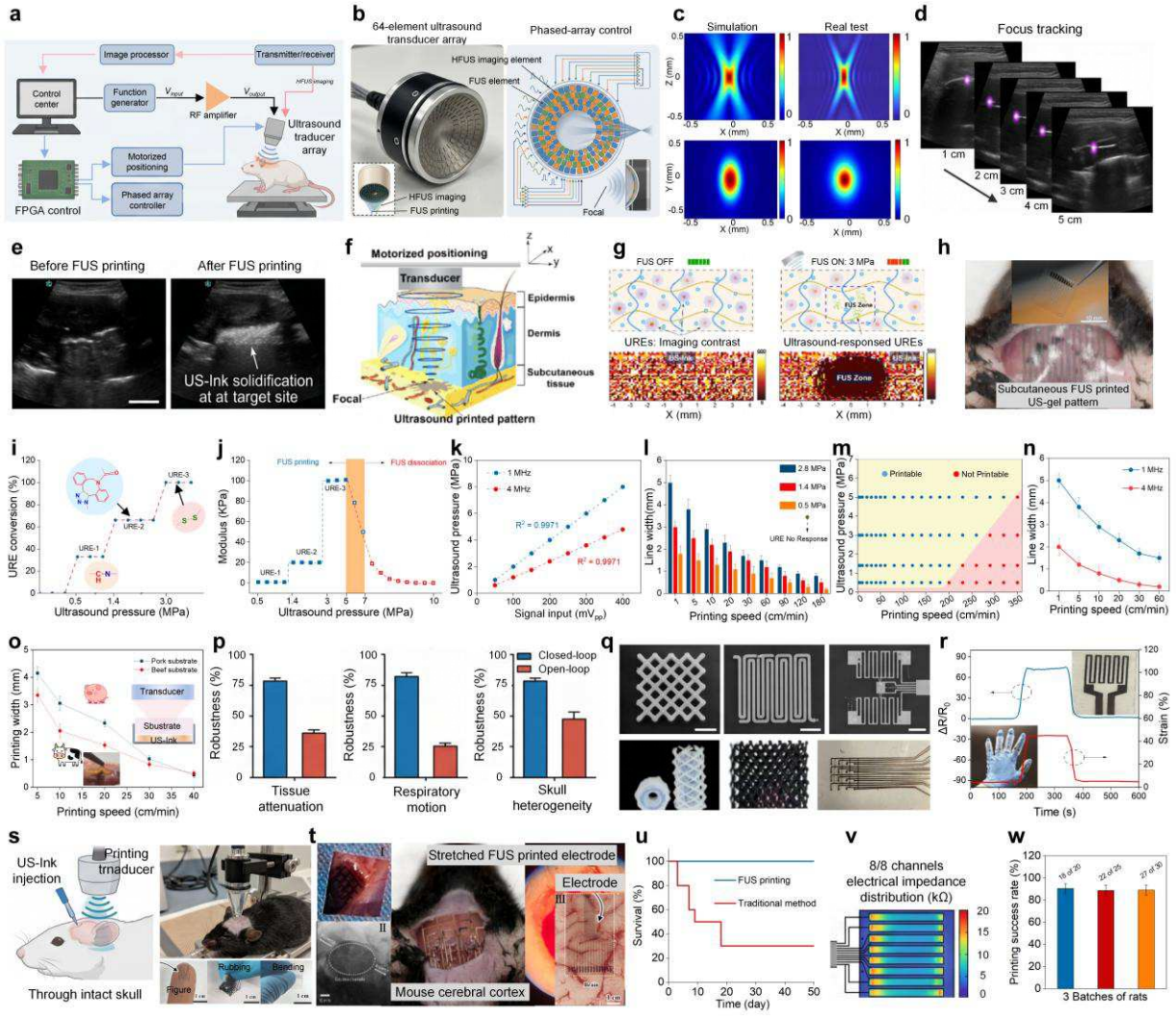


Fig. 3. Integrated ultrasound imaging–guided focused-ultrasound printing enables in vivo acoustic manufacturing. **a**, Architecture of the closed-loop ultrasound printing platform integrating focused-ultrasound actuation, ultrasound imaging, image processing, phased-array control, motorized positioning, and feedback regulation. **b**, Photograph and schematic of the 64-element phased-array ultrasound transducer. The phased array enables electronically steered focused-ultrasound printing, whereas high-frequency ultrasound imaging provides anatomical mapping and focal tracking. **c**, Normalized acoustic-pressure maps at the focal zone generated by a 1.88-MHz transducer. Experimental hydrophone measurements and simulated pressure fields are shown in the x–z plane. **d**, High-frequency ultrasound imaging of focal tracking at different printing depths. **e**, Ultrasound imaging of in vivo focused-ultrasound printing traces. **f**, Schematic of minimally invasive subcutaneous printing using AiUP. **g**, Schematic of focal-zone US-Ink crosslinking during focused-ultrasound activation and corresponding AM-mode high-frequency ultrasound images used to monitor ink distribution and focal position in vivo. **h**, Photograph of a focused-ultrasound–printed pattern recovered from the in vivo printing site. Inset, peeled printed

structure. Scale bar, 1 cm. **i**, In vivo URE conversion ratio under different ultrasound pressures. Insets illustrate pressure-dependent formation of different crosslinking networks. **j**, Storage-modulus profile defining the acoustic-pressure window for focused-ultrasound printing and the pressure range that induces dissociation of printed US-gels. **k**, Calibration of acoustic pressure as a function of input power in the AiUP system. **l**, Printing resolution, quantified by line width, using a 1.88-MHz transducer array at different acoustic powers and printing speeds. **m**, In vivo printability map of US-Ink under different acoustic powers and printing speeds. **n**, In vivo printing resolution at 1.5 MPa under different ultrasound frequencies and printing speeds. **o**, Ex vivo printing resolution on pork and beef substrates at different printing speeds. **p**, Printing robustness under different acoustic-distortion conditions with closed-loop or open-loop control. **q**, In vitro printed scaffold and electrode-like structures, and hierarchically printed catheter-like structures fabricated using AiUP. **r**, Sensitivity and reversibility of an AiUP-printed strain sensor. **s**, Schematic and representative image of in situ cortical BCI electrode fabrication using AiUP in a mouse model. Lower panels show the mechanical flexibility of the printed electrode array. **t**, Dissection images of AiUP-printed electrodes on the mouse cerebral cortex. Insets show a stimulation electrode, ultrasound imaging of an in vivo electrode, and an electrocorticography electrode on the cortex. **u**, Survival of mice after cortical electrode printing under optimized conditions. n = 20 mice. **v**, Channel yield of in vivo printed ECoG electrodes. **w**, Printing success rate across three independent rat batches. Data are shown as mean ± s.d.

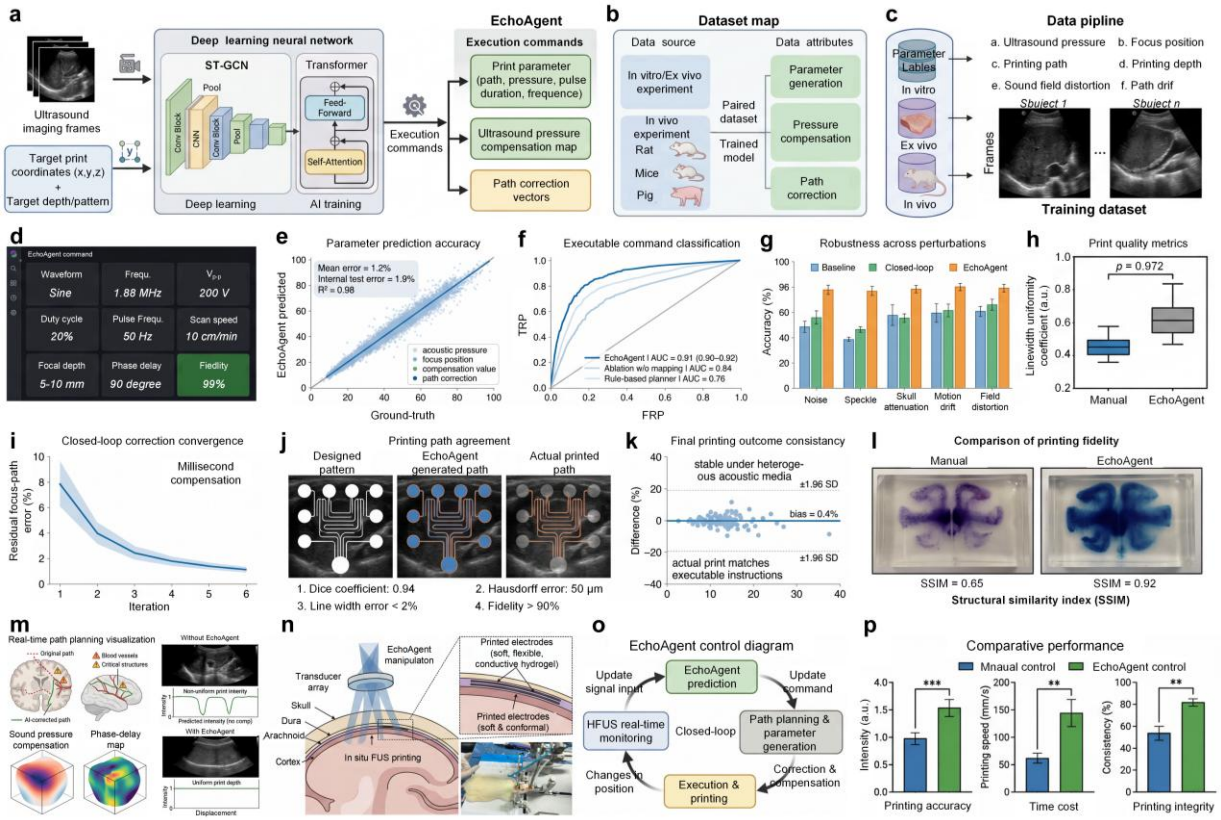


Fig. 4. EchoAgent enables closed-loop AI control of focused-ultrasound in situ printing. **a**, Architecture of EchoAgent. A mixture-of-experts feature extractor generates multilevel features from ultrasound images, which are aligned with printing parameters and processed by spatiotemporal graph convolutional networks. The resulting representations are passed to a

Transformer-based command generator that predicts executable AiUP printing commands. A contrastive learning branch improves image–parameter alignment. **b**, Dataset map used for EchoAgent training and evaluation. **c**, Data pipeline for spatiotemporal graph convolutional learning from ultrasound-guided printing sequences. **d**, EchoAgent dashboard displaying real-time ultrasound images, predicted commands, and printing parameters. **e**, Zero-shot prediction of printing parameters compared with labeled experimental parameters. **f**, Receiver operating characteristic curves comparing focused-ultrasound printing strategies. FPR, false-positive rate; TPR, true-positive rate. **g**, Robustness of different focused-ultrasound printing strategies under perturbations include noise, motion, and acoustic distortion. **h**, Print-quality metrics comparing manual and EchoAgent-controlled focused-ultrasound printing. **i**, Convergence of closed-loop correction error during EchoAgent-controlled printing. **j**, Agreement among designed paths, predicted paths, and printed paths during AiUP. **k**, Consistency of final printing outcomes under EchoAgent control. **l**, Printing fidelity achieved by manual and EchoAgent-controlled printing. **m**, Schematic of EchoAgent-based path prediction and acoustic-pressure compensation, with high-frequency ultrasound images showing printing outcomes with or without EchoAgent. **n**, Schematic and representative photograph of in situ BCI electrode fabrication using EchoAgent-controlled AiUP. **o**, Closed-loop EchoAgent workflow, including ultrasound-image acquisition, target recognition, path planning, pressure compensation, focused-ultrasound execution, feedback imaging, and iterative correction. **p**, Comparison of manual and EchoAgent-controlled printing in accuracy, time cost, and structural integrity. Data are shown as mean ± s.d.

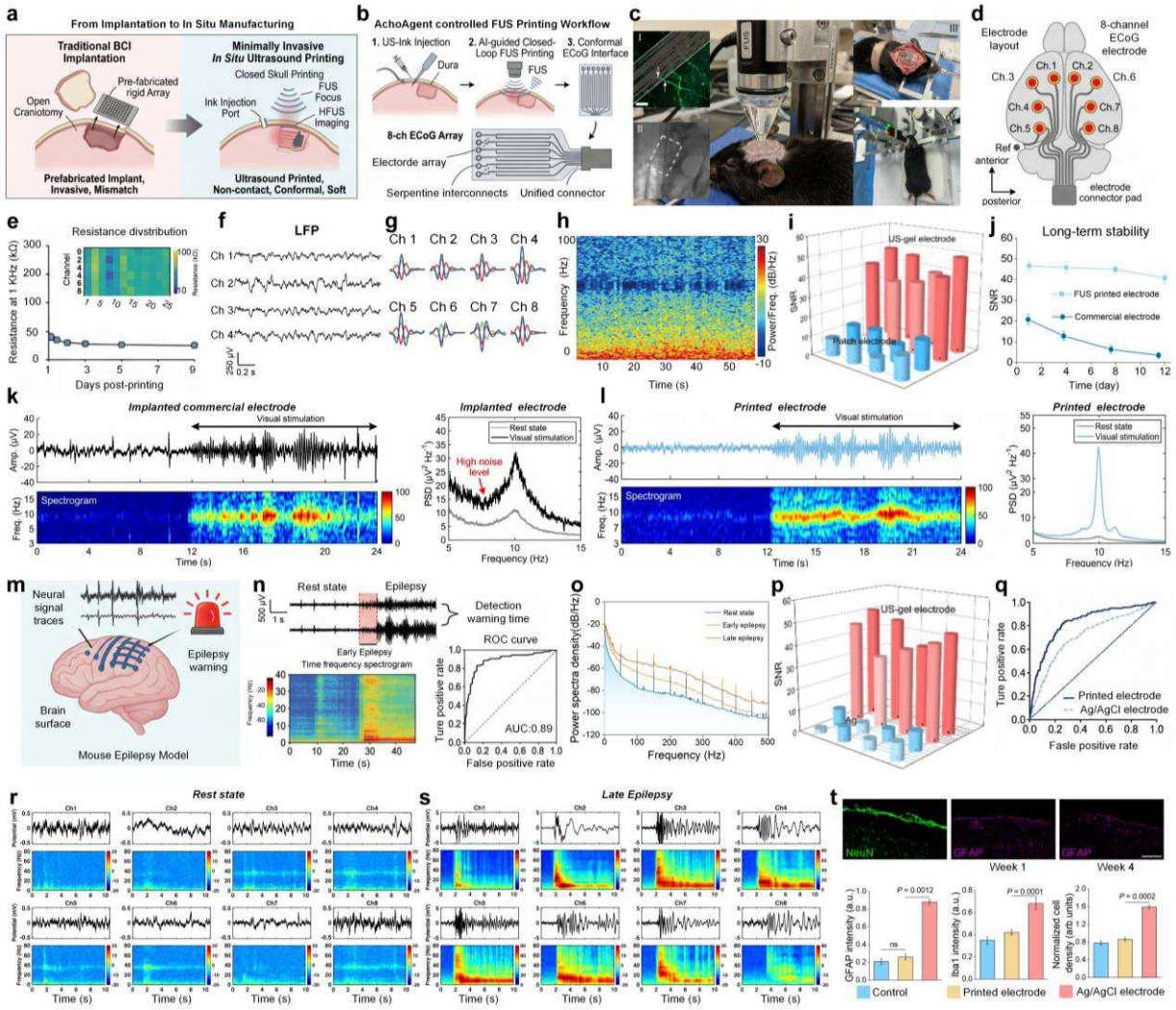


Fig. 5. AiUP prints conformal electrocorticography electrodes in rodents. **a**, Schematic of the transition from prefabricated electrode implantation to in situ neural-interface manufacturing. Conductive US-Ink is minimally delivered and then patterned by noncontact focused ultrasound to form a soft, conformal electrode array directly on the cortical surface. **b**, EchoAgent-controlled workflow for in situ BCI fabrication, including US-Ink localization, cortical-surface mapping, focal-path planning, printing-depth selection, and design of recording sites, serpentine interconnects, and connector pads. **c**, AiUP printing process in a mouse model. Insets show fluorescence imaging of the printed electrode in vivo, high-frequency ultrasound monitoring during printing, dissection of the printed ECoG electrode, and a printed electrode on the left hemisphere of the mouse brain. **d**, Schematic of ECoG channel distribution on the rat cortex. **e**, Resistance stability of printed ECoG electrodes over time. Inset shows long-term resistance stability. f, Local field potentials recorded by printed electrodes. **g**, Spike waveforms recorded by printed US-gel electrodes in rats. **h**, Time–frequency spectrogram of local field potential power from selected electrode channels. **i**, Signal-to-noise ratio of AiUP-printed US-gel electrodes compared with commercial patch electrodes. **j**, Long-term signal stability of US-gel electrodes assessed by signal-to-noise ratio. **K and l**, Motion-artifact evaluation during ECoG recording using printed US-gel electrodes and commercial invasive soft electrodes. Representative ECoG traces and corresponding spectrograms are shown during resting state and visual stimulation. **m**,

Schematic of the mouse epilepsy model used to evaluate printed electrodes. **n**, Representative local field potential recordings during resting and epileptic states and corresponding time–frequency spectrograms. **o**, Power spectral density of local field potentials in different brain states. **p**, Signal-to-noise ratio of local field potentials recorded by printed electrodes and Ag electrodes during early epilepsy detection. **q**, Receiver operating characteristic analysis comparing early seizure-warning performance of printed electrodes and Ag electrodes. **r** and **s**, Representative multichannel local field potential recordings and corresponding time–frequency spectrograms during resting state and late epileptic state. **t,** Biosafety evaluation of printed electrodes. Immunofluorescence images of rat brain slices after electrode printing show NeuN-positive neurons and GFAP-positive glial cells. Data are shown as mean ± s.d.

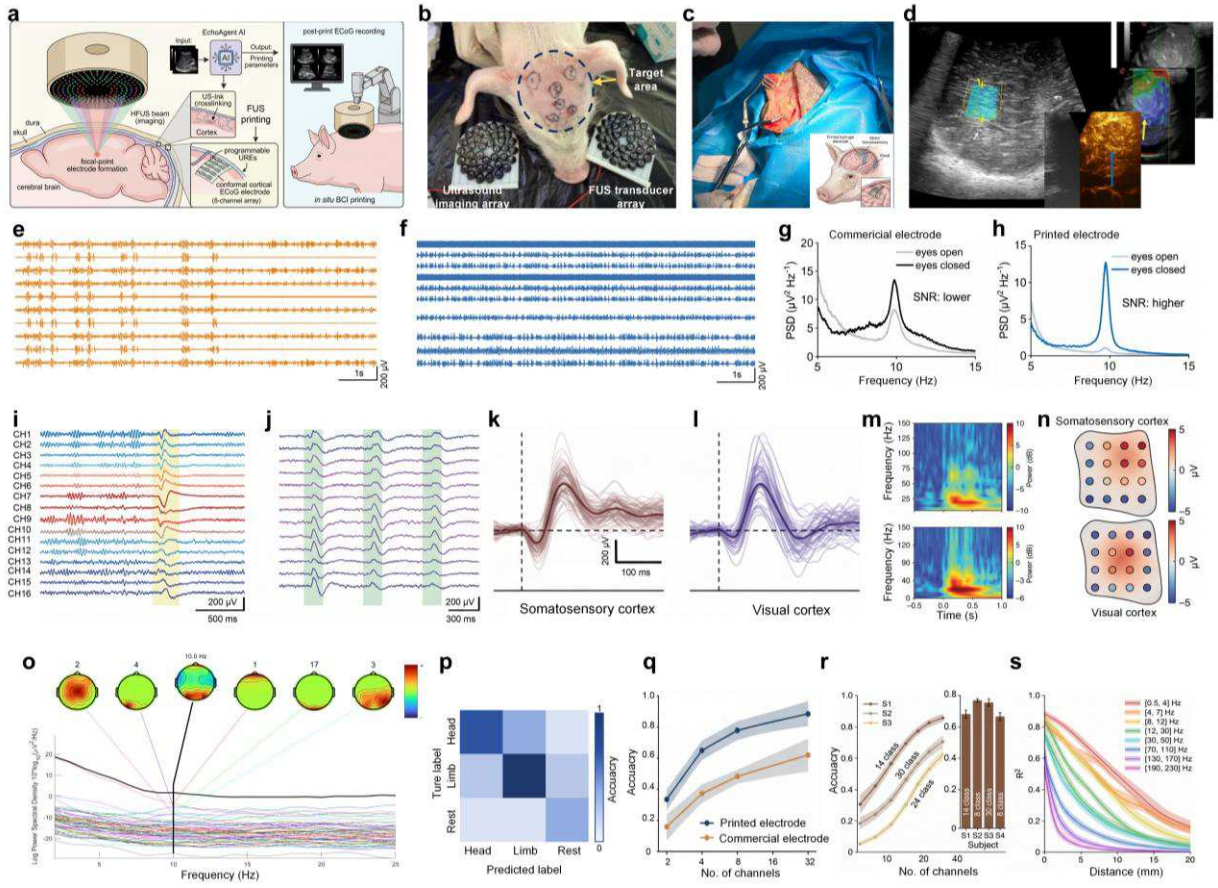


Fig. 6. AiUP enables large-animal cortical recording and neural decoding in pigs. **a**, Schematic of the AiUP workflow for in situ cortical electrode fabrication in a pig model. **b**, Representative image of the electrode printing process in a pig. **c**, Photograph of the cortical electrode printed in a pig. Inset schematic of printed electrode placement over porcine somatosensory and visual cortices for ECoG recording and decoding. **d**, Ultrasound imaging of electrode formation during AiUP and simultaneous focal-point tracking. **e** and **f**, Representative EEG signals recorded from AiUP printed subcutaneous electrodes in a pig under anesthesia and awake state. g and **h**, Power spectral density (PSD) analysis of EEG signals recorded using a commercial electrode (**g**) and an AiUP printed subcutaneous electrode (**h**). **i**, Representative ECoG signals recorded from a printed 16-channel electrode array during tibial nerve electrical stimulation. **j**, ECoG signals recorded from printed electrodes during visual stimulation. **k-l**, Overlaid sub-recordings and spikes analysis from (**i**) and (**j**) showing channel-dependent

differences across stimulation conditions. **m**, Time–frequency spectrograms from selected channels over the somatosensory cortex. **n**, Cortical surface voltage map reconstructed from a 16-channel printed electrode array over the left sensorimotor cortex. o, PSD analysis of signals recorded by printed electrode arrays in the pig brain, showing region-specific cortical activation. **p**, Limb-movement decoding using pre-movement neural activity, shown as a confusion matrix. **q**, Decoding accuracy of printed electrodes compared with implanted commercial electrodes. **r**, Decoding accuracy across three pigs. The number of stimulation locations differed among animals because tactile stimulation quality varied across experiments. **s**, Pearson correlation coefficients of spontaneous cortical activity as a function of electrode separation across ECoG frequency bands. Data are shown as mean ± s.d.

Supplementary Files

This is a list of supplementary files associated with this preprint. Click to download.

- NatureNanotechsupplementarymaterials.pdf